

Fabrication and characterization of Cu–Zn–Sn shape memory alloys via an electrodeposition–annealing route

Richard Espiritu and Alberto Amorsolo Jr.

Department of Mining, Metallurgical and Materials Engineering, University of the Philippines Diliman, Quezon City 1101, Philippines
(Received: 26 November 2018; revised: 24 June 2019; accepted: 24 June 2019)

Abstract: Cu–Zn–Sn shape memory alloys (SMAs) with an average composition of 56.0at%, 36.1at%, and 7.9at% for Cu, Zn, and Sn, respectively, were successfully fabricated via an electrodeposition–annealing route. The produced SMAs were assessed for shape memory response in terms of percent displacement (martensite phase recovery) by subjecting the ternary alloys to flame tests and subsequently characterizing them via differential scanning calorimetry (DSC), optical microscopy, scanning electron microscopy in conjunction with energy-dispersive spectroscopy (SEM-EDS), and X-ray diffraction (XRD) analysis. The flame tests showed that the highest displacement was ca. 93%, with average austenite and martensitic start transformation temperature of 225°C and 222°C, respectively. XRD analysis revealed that the intermetallic phases responsible for the observed shape memory properties have substitutional Zn in the lattice occupied by Cu and Sn, leading to the formation of Cu(Zn,Sn) and Cu₆(Zn,Sn)₅ variants. The formation of these variants was attributed to the faster interdiffusion of Cu into Sn, driven by an activation energy of 34.82 kJ·mol⁻¹. Five cycles of repeated torching–annealing revealed an essentially constant shape memory response, suggesting that the fabricated SMAs were consistent and sufficiently reliable for their intended service application.

Keywords: electrodeposition; annealing; intermetallics; martensitic transformation; shape memory alloy

1. Introduction

Over the decades, there has been aggressive research on the development of novel materials that exhibit the shape memory effect (SME). These new materials have found numerous uses in manufacturing industries and are exploited to provide innovative solutions in specialized applications such as aircraft hydraulic couplings in aerospace engineering, actuators and electrical interconnects in robotics and power engineering, implant materials for orthopedic and orthodontics, and cardiovascular scaffolds and catheter guidewires for biomedical applications [1–7]. These relatively new metallic materials that exhibit SME are commonly called shape memory alloys (SMAs). Among the various SMAs, Ti–Ni-based SMAs exhibit good properties in terms of ductility, strength, and corrosion resistance, which are important considerations for their practical use, in addition to superb SME characteristics [5,8–10]. However, they are very expensive compared with Cu-based SMAs, which are a

favorable alternative to Ti–Ni-based SMAs because of their comparable mechanical properties [11–12].

Among the Cu-based SMAs, two groups are being developed for practical application: CuZn-based and CuAl-based ternary alloys [1,13–14]. CuZn-based ternary alloys are highly ductile compared with other Cu-based alloy systems and resist fractures at grain boundaries, hence, they are the preferred alloys among the Cu-based SMAs ready for practical application [15–16]. However, most commonly produced Cu-based SMAs, such as Cu–Zn–Al and Cu–Ni–Al, undergo a phase transformation at temperature less than 100°C [17]. Binary CuZn alloy (brass) can exhibit a complete SME within a narrow composition range (38.5wt%–41.5wt% Zn) but also exhibit a very low martensitic transformation temperature (–180°C to –10°C) [1,15]. This low martensitic transformation temperature effectively hinders the use of Cu-based SMAs under high-temperature service conditions and limits their use to low-temperature environments [18]. Many industries, including the aerospace,

Corresponding author: Richard Espiritu E-mail: richard.espiritu@coe.upd.edu.ph

© University of Science and Technology Beijing and Springer-Verlag GmbH Germany, part of Springer Nature 2019

defense, and engineering fields, will greatly benefit from the use of high-temperature SMAs. Hence, their transformation temperature needs to be adjusted by adding a third element such as Al, Si, Sn, Mn, or Zr [19–21]. The transformation temperature is highly dependent on the alloy composition [12–13] as well as the quenching rate [19].

The electrodeposition technique has been previously reported as a method of producing Ti–Ni [22] and Cu-based SMAs, however, it requires elaborate plating chemistries involving, for example, ionic liquids [23] and has been optimized only for two-component (binary) alloys [24]. The present study focuses on the characterization of Cu–Zn–Sn SMAs fabricated by an electrodeposition–annealing method using a facile sulfuric acid–sulfate bath and utilizing Cu–Zn strips as a base alloy substrate. Such a process of synthesizing SMAs avoids the use of expensive metal powder precursors, provides the benefit of not involving a melting process typically used in the commercial production of SMAs, and also avoids the use of costly forming equipment—specifically, rolling and machining equipment, ball-milling equipment, or a melt spinning facility [17,25–30]. In addition to affecting the SME property, the addition of Sn to Cu–Zn alloy has also been reported to enhance the corrosion resistance of the resulting ternary alloy [31].

2. Experimental

2.1. Sample preparation

Commercially procured shim brass was cut into 8 cm × 2 cm strips using a paper cutter, and a portion of the initial shim brass was set aside for compositional analysis. The initial thickness of the brass strip was measured using a Mitutoyo 293-831 digimatic micrometer caliper. Each side of the strip was subjected to manual grinding using 400 grit sandpaper under flowing water to remove dirt and oxides on the brass surface and to ensure optimum deposition during Sn electroplating. The initial weight of the shim brass and its weight after polishing were measured on a Shimadzu AUX-320 analytical balance.

2.2. Direct-current Sn plating

2.2.1. Preparation of the plating bath

The sulfuric acid–sulfate plating bath used in the experiments was based on the recipe of Schlesinger and Pautovic [32] with modifications. To prepare the Sn plating bath, a precalculated amount of tin(II) sulfate (SnSO_4) was dissolved in distilled water to a concentration of 45 g·L⁻¹. Subsequently, 2 g of gelatin was added. Afterwards, an appropriate amount of concentrated sulfuric acid (H_2SO_4) was

slowly added to the bath solution to obtain a concentration of 150 g·L⁻¹ with continuous stirring until the plating bath cooled to room temperature.

2.2.2. Electrodeposition of Sn on brass

Pure Sn (99.9%) was connected to the positive terminal (anode), and the polished brass substrate was connected to the negative terminal (cathode) of an Extech Instruments 382213 DC regulated power. An insulating adhesive tape was placed on one side of the pre-weighed brass strip to ensure a constant plating area of 6 cm × 2 cm. The weight of the taped brass strip prior to plating was recorded. The brass substrate and the Sn anode were both immersed in the plating bath 2 cm apart. Plating commenced immediately after the current was set to 20 mA with the other operating parameters (Table 1) to obtain the target sample of 13wt%, 26wt%, 39wt%, and 46wt% Sn as computed relative to the mass of the plated brass substrate. One side of the brass strip was initially insulated with adhesive tape and subsequently removed and turned over after half of the total plating time had elapsed. This method was used to ensure that the plating thickness on both sides of the brass substrate was approximately equal. After deposition of the desired amount of Sn, the Sn-plated brass strip was removed from the bath and washed with copious amount of water. The plated strip was allowed to dry and subsequently weighed to measure the amount of Sn deposited. The final thickness of the strip was measured, and a portion of the Sn-plated brass was set aside for compositional analysis.

Table 1. Operating parameters of the modified sulfuric acid–sulfate bath

Parameter	Setting value
Current density / (mA·cm ⁻²)	0.83
pH	0.3
Bath temperature	Room temperature
Agitation / (r·min ⁻¹)	60

2.3. Thermal alloying of Sn-plated brass strip

The Sn-plated brass strips were subjected to a thermal alloying or annealing treatment at different temperature (i.e., 350, 380, 400, and 420°C) for 120 min. Each strip was placed standing laterally (using a ceramic brick support) in an alumina boat and then placed in a Carbolite MTF 12/38/250 tube furnace with a constant ramping rate of 50°C·min⁻¹. The tube furnace was pre-purged with nitrogen, after which the same nitrogen gas was allowed to continuously flow through the tube during annealing (i.e., to ensure the absence of oxygen).

2.4. Quenching

To investigate the effect of quenching conditions on the shape memory response of the fabricated ternary alloy, the metal strips after annealing at 380°C under ambient nitrogen were immediately quenched (rapidly cooled) using two quenching media, i.e., ice-water and water, at room temperature (23°C). A portion of the quenched metal strip was set aside for analysis.

2.5. Characterization of the Cu–Zn–Sn alloy strips

2.5.1. Compositional analysis

Samples were subjected to X-ray fluorescence (XRF) analysis using a Shimadzu EDX-720 X-ray spectrometer to determine the percent composition of each component. The alloy strips were also analyzed using a Shimadzu XRD-7000 X-ray diffractometer equipped with a Cu-K α radiation source; the samples were scanned from 10° to 90° to identify the phase and to verify the presence of metastable phase in the annealed metal samples.

2.5.2. Microstructural analysis

A portion of each sample was mounted on a resin and was subsequently polished. The iron(III) chloride (FeCl₃) etchant was prepared by dissolving 25 g of FeCl₃ in 25 mL of concentrated hydrochloric acid and 50 mL of ethanol [33]. After the etchant treatment, the microstructure of the etched samples was analyzed using a Leica DMRME optical microscope.

To prepare the sample for electron microscopic analysis, polished metal samples were initially sputtered with Au using a JEOL JFC 1100 ion sputtering system with an Au target. Scanning electron microscopy (SEM) analysis of the Au-coated samples, in conjunction with energy-dispersive spectroscopy (EDS), was performed using a JEOL JSM-5310 scanning microscope.

2.5.3. Test for SME

The quenched metal strips were subjected to a flame test in order to visually confirm whether the samples demonstrate a shape memory response. Each originally straight and flat strip was bent into a circular arc orientation and firmly mounted onto a test frame. A Sony DSC W300 digital video camera was used to record the response of the metal strip upon application of the flame from a pencil torch. Frame captures of the initial state and responses of the metal strip to heat were then superimposed using the Google Picasa software to conveniently measure the percent displacement. Fig. 1 shows the superimposed images of the alloy sample after flame test and the formula used to calculate the percent displacement.

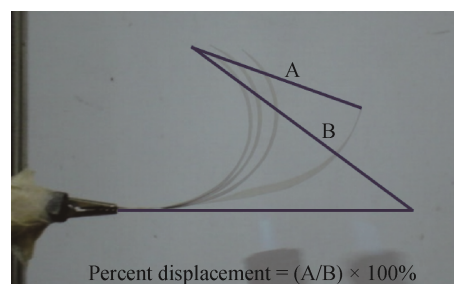


Fig. 1. Superimposed images of the response of the alloy strip to a flame.

2.5.4. Thermal cycling

The effect of repeated tests for SME was also investigated wherein Sn-plated ternary alloy annealed at 400°C for 120 min was quenched in tap water (26°C) and subsequently pencil torched and re-annealed/quenched for five cycles. The response of the strip with the pencil torch flame was recorded for each cycle (Fig. 1) and then processed for comparison.

2.5.5. Thermal analysis

The alloy strips were subjected to differential scanning calorimetry (DSC) analysis using a TA Instruments DSC Q10 to determine the austenitic (A_s = start; A_f = finish) and martensitic (M_s = start; M_f = finish) transformation temperature. Samples for DSC analysis with diameter of 3 mm were prepared using Gatan model 659 disk punch. The temperature scan range was 0°C to 400°C with heating hermetically at a 5°C·min⁻¹ ramp rate and cooling to 30°C at a 3°C·min⁻¹ ramp rate.

3. Results and discussion

3.1. Compositional analysis

XRF spectrometric analysis confirmed that the shim brass substrate had a normalized composition of 64.9wt% Cu and 35.1wt% Zn and, hence, a Cu-to-Zn weight ratio of 1.85. The calculated elemental ratios of the metal constituents in the as-plated and annealed samples are shown in Table 2. The Cu-to-Zn ratio decreased with increasing amount of electrodeposited Sn. In the case of the annealed samples, the Cu-to-Zn ratios were essentially constant at 2.0. The results (Table 2) also indicated that alloying occurred between the Sn and the brass layer because the Sn-to-(Cu and Zn) ratio of the annealed sample was smaller than that of the corresponding as-plated sample at the same composition. The increasing Sn-to-(Cu and Zn) ratios were also attributable to the increasing amount of unreacted Sn on the surface of the alloyed strip.

Table 2. XRF elemental ratios for the as-plated and annealed Sn-plated brass

Materials	Sn / wt%	Cu/Zn	Sn/(Cu and Zn)
Sn-plated brass	13	1.6	0.5
	26	1.3	3.6
	39	1.3	30.6
	46	1.1	34.6
Annealed Sn-plated brass	13	2.1	0.4
	26	2.2	1.4
	39	2.0	4.0
	46	1.9	5.5

3.2. Microstructure analysis

3.2.1. Unetched ternary alloy

Fig. 2 shows optical micrographs of the as-plated and annealed Cu–Zn–Sn strips obtained at 500X magnification. The electrodeposition of Sn was uneven and generally thickened with increasing Sn amount. In the annealed samples, interdiffusion of the metal constituents was observed, where a new layer of Cu–Zn–Sn intermetallic was formed as the central brass layer was consumed.

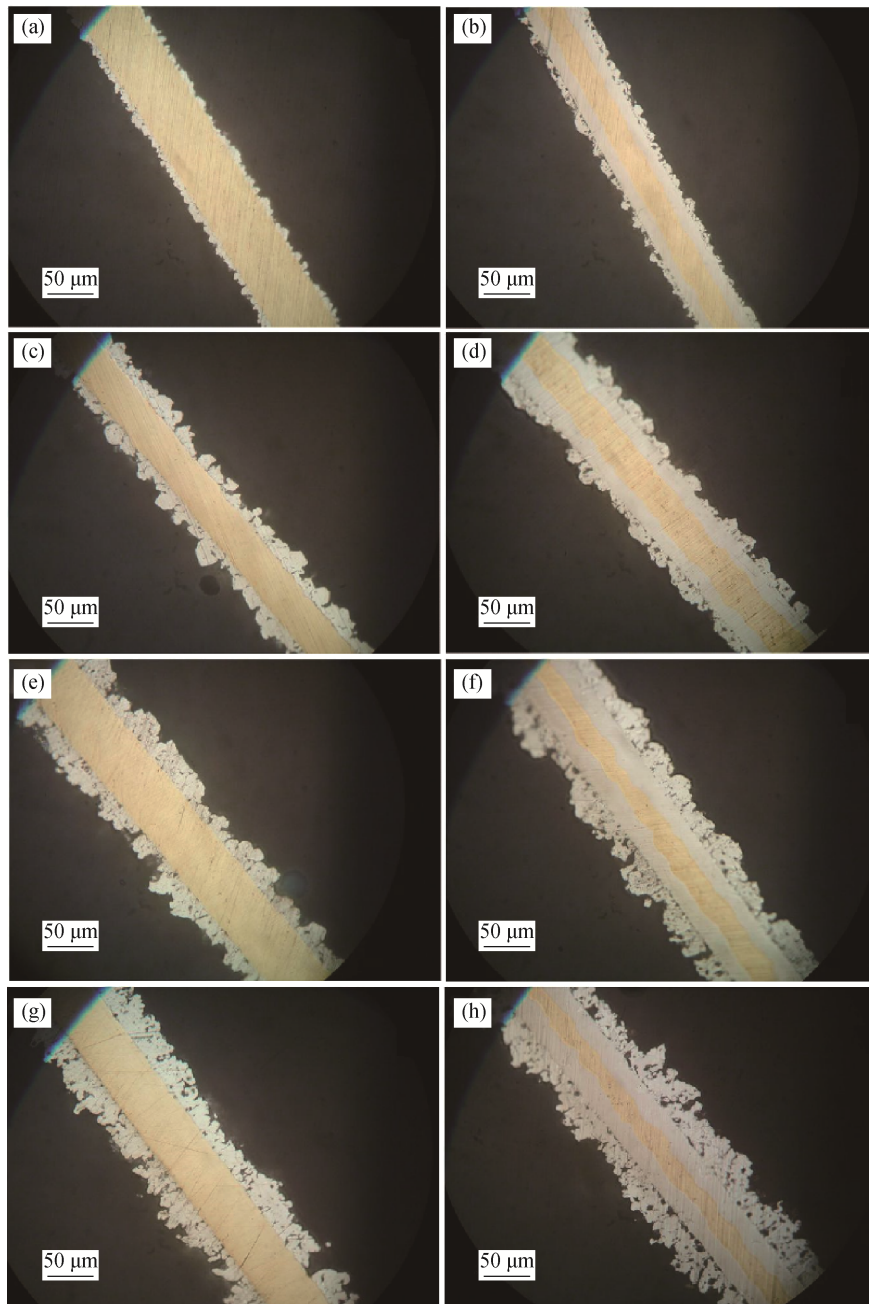


Fig. 2. Optical micrographs of (a,c,e,g) before and (b,d,f,h) after annealing of metal strips with 13wt%, 26wt%, 39wt%, and 46wt% Sn, respectively.

A comparison of the as-plated and annealed samples revealed that annealing produced distinct intermetallic layers between the electrodeposited Sn and the brass substrate. The unreacted outer layer of Sn appeared to become more porous because of the escape of trapped gases during annealing. The transformation into a porous structure was due to the formation of molten Sn phase at high temperature based on the Cu–Sn phase diagram, which increased the solubility of gas in this phase. During rapid quenching, the decrease in solubility will lead to nucleation of excess

gases, which can become trapped in the layer after solidification.

3.2.2. Etched ternary alloy

Fig. 3 shows the microstructure of the etched annealed Sn-plated brass strips, as observed using an optical microscope. The diffusion of the intermetallic layer on both sides of the brass substrate (center) was evident in the optical micrographs. The intermetallic layers were assumed to be the interdiffusion sites of Sn, with Cu and Zn moving in the opposite direction.

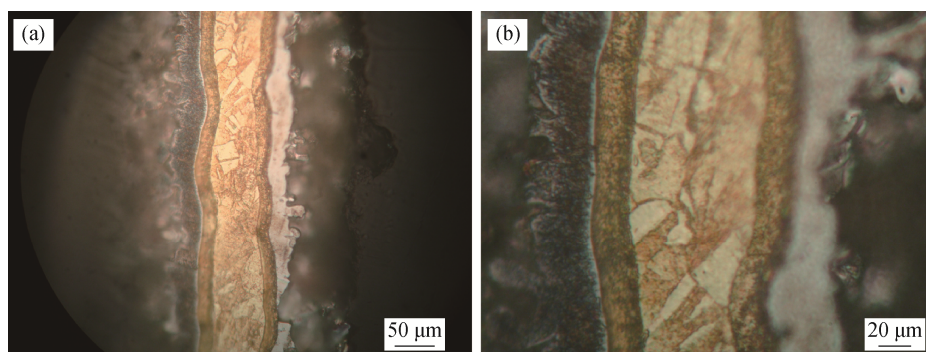


Fig. 3. Optical micrographs of etched annealed Sn-plated samples Sn-plated samples at different magnification.

The presence of fine grains in the brass layer indicated recrystallization upon annealing treatment of the deformed grains in the as-received brass. We also observed that the unreacted brass layer appeared to be composed of a combination of lighter and darker grains, which could mean that the grains have different crystal orientations that result in different etching rates among the grains or that the grains differ in composition. The formation of the β' -brass phase can produce grains whose physical appearance in the optical micrographs differed from those of grains of α -brass because β' -brass grains had a higher Zn content than α -brass grains. On the basis of the Cu–Zn phase diagram, the composition of the starting brass predicts the microstructure to be predominantly composed of grains of α -brass, along with some grains of β' -brass.

3.3. SEM-EDS analysis of Cu–Zn–Sn strips

SEM imaging coupled with EDS analysis were performed on the cross-section of alloy samples to provide higher-magnification images of the microstructures and to obtain accurate measurements of the composition of each metal component and the newly formed intermetallic layer. Fig. 4 shows an SEM micrograph of the initial shim brass sheet using secondary electrons. The EDS analysis revealed an average brass composition of 64.3wt% Cu and

35.7wt% Zn, which agreed well with the XRF analysis results.

The as-plated Sn on brass and the annealed Cu–Zn–Sn strips were analyzed, and the micrographs were captured using backscattered electrons (BSEs), as shown in Fig. 5. The use of the BSE imaging technique provides a contrast helpful in distinguishing the presence and identifying the distinct layers in the microstructure. In BSE imaging, a phase containing elements with higher atomic numbers will appear brighter than a phase containing elements with lower atomic numbers. Hence, the brightest layer is the one with highest Sn content, whereas the darkest layer (at the center) is the one with minimal Sn content (i.e., the CuZn substrate). The fact that the brass appeared homogeneous suggested that the base alloy had essentially a single-phase composition. As shown in Fig. 5(a), the plated Sn on the brass surface was not perfectly planar, as similarly observed in the optical micrographs (Fig. 2), and the deposited crystals exhibited dendritic character, resulting in porosity and surface roughness in the plated region. Even though the electrodeposition of Sn on the brass surface was not uniform, there was no observed delamination or loss of adhesion of the newly formed intermetallic layer and the exposure to high temperature during annealing even resulted in an alloy having planar intermetallics between the Sn and the brass layer,

as shown in Fig. 5.

Figs. 5(b) and 5(d) are SEM micrographs of alloy samples annealed at different temperature but with essentially the same bulk composition of ca. 26wt% Sn. At high annealing temperature, the homogeneity of the intermetallic layer in terms of its composition improved. The presence of voids in the outer layers was also prominent in the sample

annealed at 420°C because the faster interdiffusion of Cu and Sn compared with that Zn caused a decrease in the thickness of the brass layer. In addition, for alloyed samples annealed at high temperature (Figs. 5(e) and 5(f) [34]), two phases were observed in the outermost layer, which included a Sn-rich region (position 3) and another phase with substantial Cu and Zn contents (position 4).

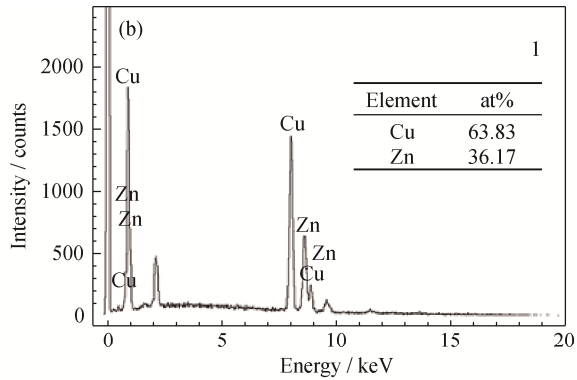
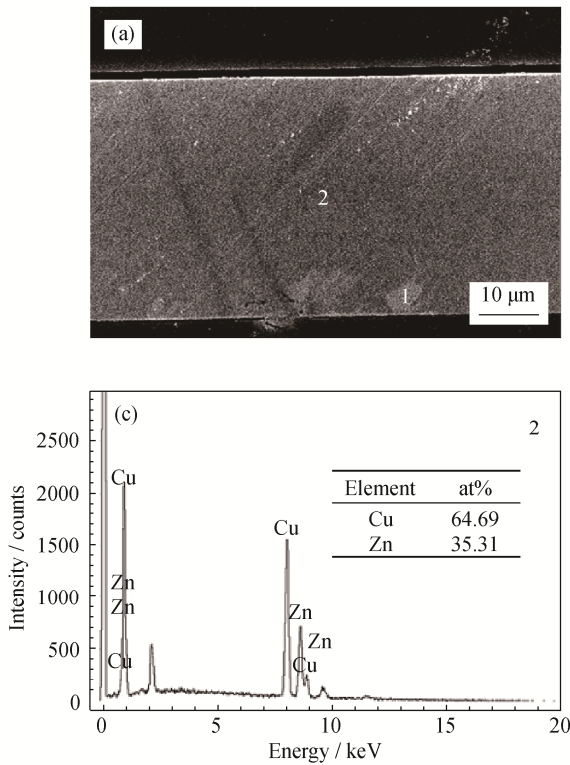


Fig. 4. SEM-EDS analysis results for the initial shim brass: (a) SEM image; (b,c) the corresponding EDS analysis to point 1 and 2, respectively.

Table 3 summarizes the intermetallic layer composition on either side of the unreacted brass. The intermetallic layers (positions 1 and 2) are those attributed to the shape memory behavior of the fabricated ternary alloys. On the basis of EDS results, the intermetallics had an average content of 7.9at% Sn, consistent with reports in the literature for the Cu–Zn–Sn SMA [1–2,15]. Finally, the average composition of the fabricated SMA was 56.0at%, 36.1at%, and 7.9at% for Cu, Zn, and Sn, respectively.

3.4. Kinetics of intermetallic layer formation

The thickness of the intermetallic layer was measured from the micrographs, wherein the fraction of intermetallics in the strip was determined by computing the ratio of intermetallic thickness over the bulk alloy thickness. The effect of increasing annealing temperature on the thickness of intermetallics in the alloyed strip was measured at a constant annealing time of 120 min under a N₂ atmosphere.

Fig. 6 shows excellent linearity of the intermetallic thickness with increasing annealing temperature. At essentially constant Sn content, as the annealing temperature increased, the thickness of the resulting intermetallic layer also increased. As previously mentioned, this increase in thickness essentially translated to improved shape memory response.

The presence of an intermetallic phase between the CuZn alloy and Sn metal layers can greatly affect the interdiffusion rates because new and different structures of intermetallics from the pure metal constituents are formed. These intermetallic compounds exist because they have lower free energies than the terminal solids, which makes the formation of these phases favorable. During annealing, these thermodynamically stable phases become even thicker until, ideally, all the pure metals are consumed. Data pertaining to the variation of the intermetallic thickness with time at different temperature can provide useful

information in describing the kinetics of the intermetallic growth in the diffusion layer. From Fig. 6, we can determine the activation energy using the following empirical formula [35]:

$$y = x_0 + At^n \exp\left(-\frac{Q}{RT}\right) \quad (1)$$

where y is the intermetallic layer thickness at time t , x_0 is the initial intermetallic thickness, A is a numerical constant, n is the rate-determining exponent, and Q , R , and T are the empirical activation energy, gas constant, and the annealing temperature (in Kelvin), respectively. Because no initial in-

termetallic layer was present before alloying ($x_0 = 0$), eq. (1) reduces to

$$y = At^n \exp\left(-\frac{Q}{RT}\right) \quad (2)$$

By plotting $\ln y$ versus $1/T$ based on the annealing runs, the empirical activation energy (Q) can be computed from the slope of the graph. Fig. 7 reveals excellent linearity, indicating adherence to the empirical relationship and consistent with first-order solid-phase martensitic transformation kinetics, where the computed slope leads to an estimated Q of $34.82 \text{ kJ}\cdot\text{mol}^{-1}$.

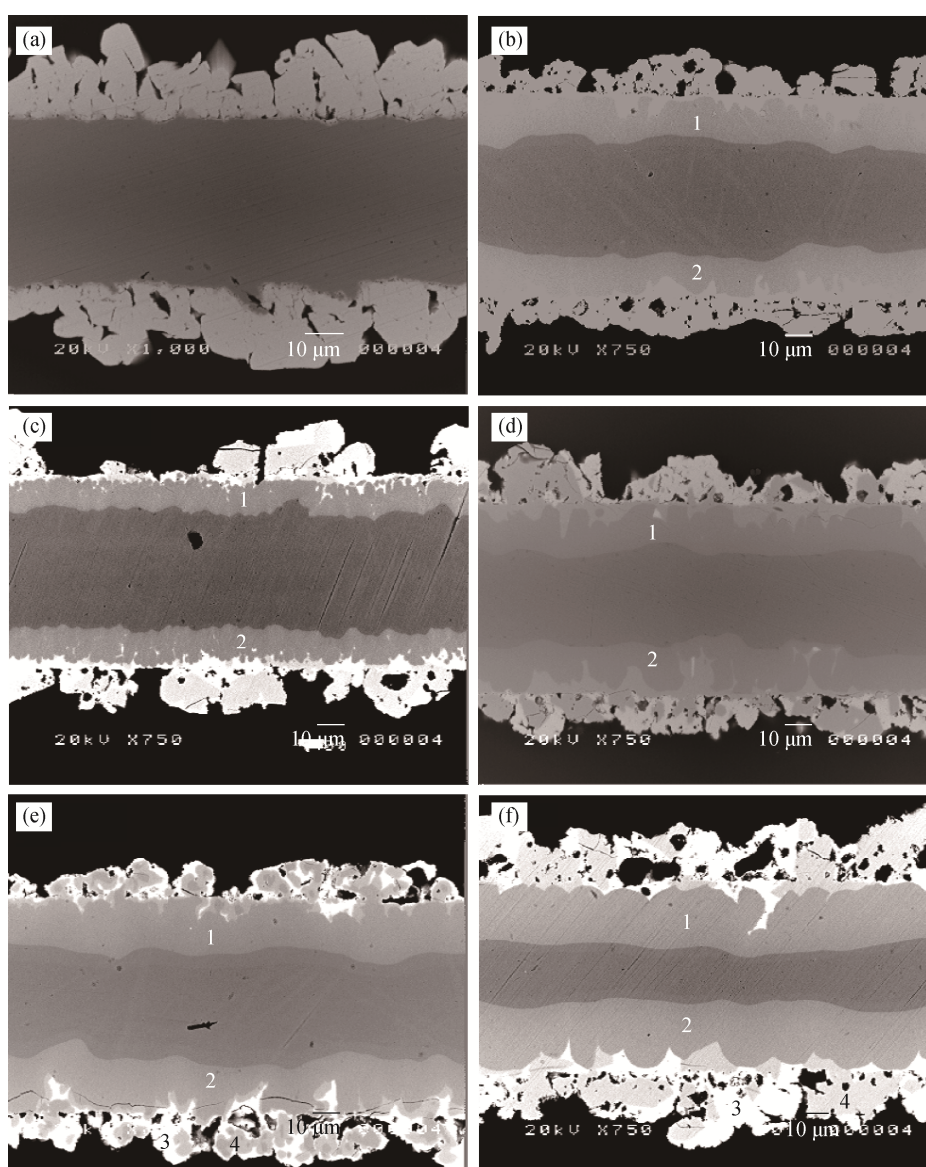
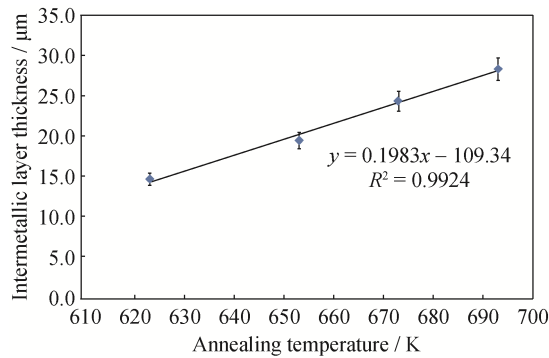
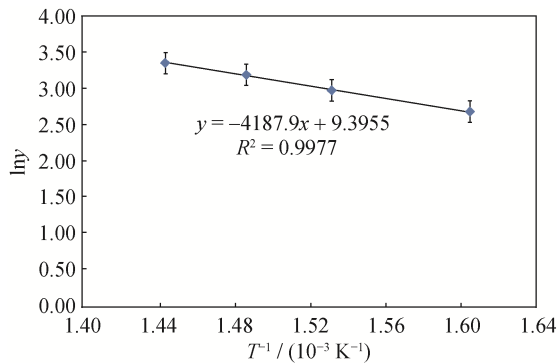


Fig. 5. SEM micrographs at 750X magnification: (a) unannealed Sn-plated brass; (b) AL-1 annealed at 380°C; (c) AL-2 annealed at 350°C; (d) AL-3 annealed at 400°C; (e) AL-4 annealed at 400°C; (f) AL-5 annealed at 420°C. (f) Reprinted by permission from Wiley-VCH Verlag GmbH & Co. KGaA A Company of John Wiley & Sons, Inc.: *Microscopy and Analysis*, SEM-EDX analysis of intermetallic phases in a Cu–Zn–Sn shape memory alloy, R.D.V. Espiritu and A.V. Amorsolo Jr., Copyright 2010.

Table 3. Compositions of the intermetallic layers, as determined using EDS

Alloy code	Sn / wt%	Cu / at%	Zn / at%	Sn / at%	Position
AL-1	25.6	54.7	39.4	5.9	2
		55.5	35.3	9.0	1
AL-2	25.7	54.6	38.8	6.6	2
		55.0	36.1	8.9	1
AL-3	26.5	57.5	35.4	7.2	2
		55.1	36.9	7.9	1
AL-4	26.9	55.5	37.5	7.1	2
		58.0	33.3	8.8	1
AL-5	27.0	57.4	35.3	7.3	2
		57.0	32.7	10.3	1

**Fig. 6. Effect of annealing temperature on the thickness of the intermetallic layer.****Fig. 7. Plot of $\ln\gamma$ versus $1/T$ for Cu–Zn–Sn SMAs based on a constant annealing time of 120 min.**

The measured activation energy ($34.82 \text{ kJ}\cdot\text{mol}^{-1}$) is similar to the activation energy for the diffusion Cu atoms into a Sn matrix ($16.74 \text{ kJ}\cdot\text{mol}^{-1}$ to $33.07 \text{ kJ}\cdot\text{mol}^{-1}$) [36]. Because the Cu-into-Sn diffusion activation energy is the lowest among the possible combinations of metal interdiffusion, the diffusion of Cu to Sn strongly governed the formation of the intermetallic layer (i.e., Cu diffuses faster than Zn toward the Sn layer). Recall from the XRF analysis results (Table 2) that the Cu-to-Zn ratio of the initial shim brass was 1.85 and

the ratio increased to 2.0 after annealing (i.e., the Cu at% decreased substantially from 64.69at% to ca. 56at%), which is consistent with the observation that Cu diffuses faster than Zn to Sn. However, this observation did not discount Zn also diffusing to the intermetallic layer, though at a slower rate, as mentioned previously. EDS probing indeed showed Zn to be present in the intermetallic layer, not just Cu and Sn. Finally, the results suggested that optimization of the fabrication conditions of Cu–Zn–Sn SMAs via the electrodeposition route (i.e., to achieve complete interdiffusion of metal components) should focus heavily on annealing and quenching conditions.

3.5. Flame tests

The quenched ternary alloys were examined for the SME, wherein the percent displacement of the strip was computed on the basis of superimposed images gathered from each test. Zero percent displacement indicates that the alloy did not exhibit shape memory properties, whereas 100% displacement indicates that the alloy exhibited complete strain recovery.

To account for the possibility of the shim brass having an innate SME, the brass substrate was also subjected to the same thermal treatment and measured for percent displacement. The shim brass exhibited zero displacement, which verifies that the initial brass substrate had no inherent shape memory properties. The negative shape memory response of the initial shim brass also confirmed that the addition of Sn to produce the Cu–Zn–Sn intermetallics was a contributing factor in imparting shape memory properties to the annealed metal strips.

Fig. 8 shows the computed percent displacement based on the response of the Sn-brass strip with essentially constant Sn content (25wt%–26wt%) annealed at increasing annealing temperature for 120 min under a N_2 atmosphere. The heat-treated samples were all quenched in an ice-water bath. The displacement response of the Sn-brass strips confirmed the shape memory properties of the fabricated metal strips; the highest observed displacement was 92.86% (Fig. 8(d)).

3.5.1. Effect of annealing temperature

Fig. 8 shows increasing percent displacement (i.e., SME) as the annealing temperature increased. The observed increase in percent displacement was due to the thicker intermetallic phases produced with increasing annealing temperature; these phases were responsible for the shape memory property of the ternary alloy as the annealing temperature increased. The observed less than 100% recovery of the fabricated SMAs was due to the excess un-

reacted Sn on the surface and still-unreacted CuZn in the middle region (incomplete interdiffusion), which restricted

the movement of the SMAs to full recovery during the flame test.

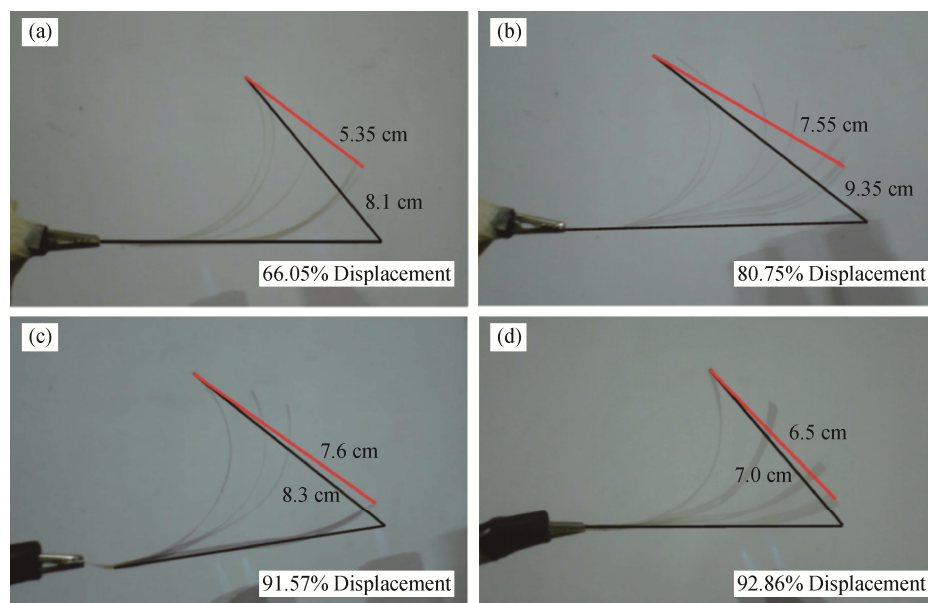


Fig. 8. Superimposed images at different conditions: (a) AL-1 annealed at 350°C; (b) AL-2 annealed at 380°C; (c) AL-1 annealed at 400°C; (d) AL-3 annealed at 400°C.

3.5.2. Effect of quenching media

Annealed AL-2 samples rapidly quenched in tap water at 23°C and an ice-water bath exhibited percent displacements of $(47 \pm 3)\%$ and $(80 \pm 4)\%$, respectively. We observed that the Cu–Zn–Sn ternary alloy quenched in an ice-water bath exhibited a substantially greater percent displacement, thus reflecting a stronger shape memory response than the strip quenched in a tap-water bath. This greater displacement was attributed to the amount of martensite phases produced being strongly dependent on the rate of quenching: the higher the rate of quenching, the greater the amount of martensite phases produced and the less austenite phase retained. As expected, using tap water as a quenching medium resulted in a lower percent displacement because not all of the parent phases were completely transformed to martensite phases.

3.5.3. Thermal cycling

The results (Table 4) show that the shape memory response of the AL-5 ternary alloy was essentially constant, as indicated by the minimal loss of the SME after five cycles. The repeated annealing–quenching–torching provided sustained shape memory properties to the ternary alloy as thermal cycling homogenizes the structure of the intermetallic layers [37]. The obtained results therefore suggested that the fabricated Cu–Zn–Sn SMA was potentially useful in industrial and commercial applications because it exhibited consistent shape memory properties even after several thermal cycling treatments.

Table 4. Percent displacement after torching–annealing–quenching cycles of the annealed AL-5 alloy

Torching–annealing–quenching cycles	1	2	3	4	5
Percent displacement	65.12	58.89	71.26	65.56	62.79

3.6. DSC analysis

DSC is widely used to determine the transformation temperature and the energies of transformation of SMAs [38]. The initial and annealed brass substrates were subjected to DSC analysis to verify that the base alloy did not exhibit SME, as suggested by the flame test. The DSC thermogram of the initial and annealed brass (Fig. 9 [39]) revealed an endothermic peak at 31.1°C that can be attributed to the loss of small amount of β' grains as it dissolved into the α phase of brass. The observed peak at 122.5°C was attributed to the recrystallization of brass that could be brought about by cold work during processing. Clearly, Fig. 9 does not show characteristic transformation temperature peaks typical for SMAs reported in the literature [2,18,40], which confirmed the results of the flame test that the brass substrate did not possess shape memory properties.

The transformation temperature of the annealed Sn-brass samples from the lowest to the highest Sn content is shown in Fig. 10 [39] and is summarized in Table 5 [39]. The observed exothermic peak (cooling curve, Fig. 10(a)) was associated with the austenite to martensite (A \rightarrow M) phase

transformation at ca. 222°C. Similarly, the recorded endothermic peaks were essentially constant at ca. 225°C irrespective of the Sn content and was attributed to the transformation from the martensite to the austenite phase (M→A) due to the formation of intermetallic phases (heating curve, Fig. 10(b)).

Table 5 also shows that each characteristic transformation temperature was essentially constant for all annealed samples. The fact that the transformation temperature was chiefly dependent on the composition suggested that the resulting intermetallic layer had essentially constant percent composition of Cu, Zn, and Sn irrespective of the amount of electrodeposited Sn. We also observed that, for the annealed samples with increasing Sn content, the ΔH of both heating and cooling increased. This increase was due to the increasing amount of Sn diffusing through the CuZn substrate, which led to an increase in thickness of the intermetallic layer. The increasing intermetallic layer thickness translated into increased formation of more parent austenite phases; thus, complete transformation to martensite phases will re-

quire a greater amount of energy. The increasing ΔH of reaction was also attributed to the increasing amount of Sn plated on the surface.

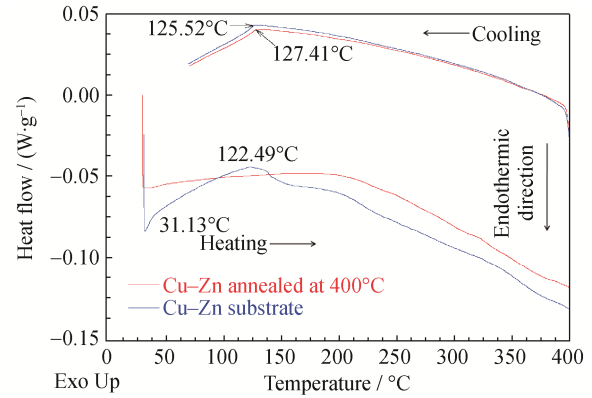


Fig. 9. DSC thermogram of the initial and annealed brass at 400°C. Reprinted by permission from Springer Nature: *Journal of Thermal Analysis and Calorimetry*, DSC analysis of Cu–Zn–Sn shape memory alloy fabricated via electrodeposition route, R.D.V. Espiritu and A.V. Amorsolo Jr., Copyright 2012.

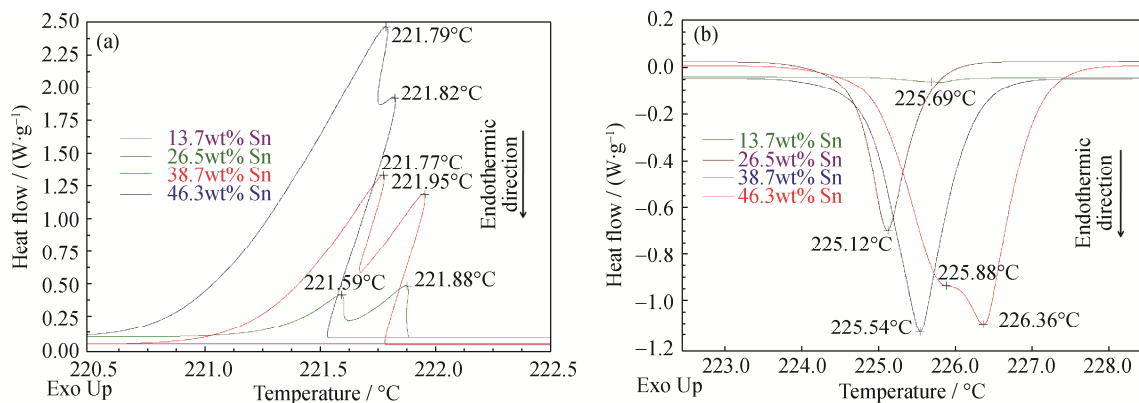


Fig. 10. DSC curves of the annealed samples with different Sn content: (a) cooling; (b) heating. Reprinted by permission from Springer Nature: *Journal of Thermal Analysis and Calorimetry*, DSC analysis of Cu–Zn–Sn shape memory alloy fabricated via electrodeposition route, R.D.V. Espiritu and A.V. Amorsolo Jr., Copyright 2012.

Table 5. Transformation temperature and energies of transformation for annealed samples with increasing Sn content. Reprinted by permission from Springer Nature: *Journal of Thermal Analysis and Calorimetry*, DSC analysis of Cu–Zn–Sn shape memory alloy fabricated via electrodeposition route, R.D.V. Espiritu and A.V. Amorsolo Jr., Copyright 2012.

Sn / wt%	$A_s / ^\circ\text{C}$	$A_f / ^\circ\text{C}$	$M_s / ^\circ\text{C}$	$M_f / ^\circ\text{C}$	$\Delta H_{\text{heating}} / (\text{J}\cdot\text{g}^{-1})$	$\Delta H_{\text{cooling}} / (\text{J}\cdot\text{g}^{-1})$
13.7	225.01	226.11	—	—	0.19	—
26.5	224.65	225.63	221.88	221.47	5.88	2.66
38.7	224.85	226.16	221.78	221.25	11.00	9.40
46.3	225.01	226.97	221.55	221.03	17.72	17.57

Table 6 [39] summarizes the transformation temperature and heat of reaction of AL-2 specimens subjected to increasing annealing temperature (350°C, 380°C, 400°C, and 420°C); the corresponding DSC thermograms are shown in Fig. 11 [39]. Similar to the results in Fig. 10, the transformation temperature was essentially constant, irrespective of the annealing temperature. For the specimens annealed at the temperature above 350°C, two very close exothermic peaks were observed in the cooling curves. These peaks could be due to the presence of two intermetallic layers (one on each side of the brass); their compositions may vary slightly, resulting in a small difference in their transformation temperature.

Table 6. Transformation temperature and energies of transformation for AL-2 samples annealed at various temperature. Reprinted by permission from Springer Nature: *Journal of Thermal Analysis and Calorimetry*, DSC analysis of Cu–Zn–Sn shape memory alloy fabricated via electrodeposition route, R.D.V. Espiritu and A.V. Amorsolo Jr., Copyright 2012.

Annealing temperature / °C	A_s / °C	A_f / °C	M_s / °C	M_f / °C	$\Delta H_{\text{heating}}$ / (J·g ⁻¹)	$\Delta H_{\text{cooling}}$ / (J·g ⁻¹)
350	224.82	225.96	221.56	221.17	10.46	7.616
380	224.83	226.09	221.74	221.21	7.698	6.267
400	224.77	225.85	221.92	221.48	6.858	4.739
420	224.67	225.82	222.13	221.37	8.415	5.977

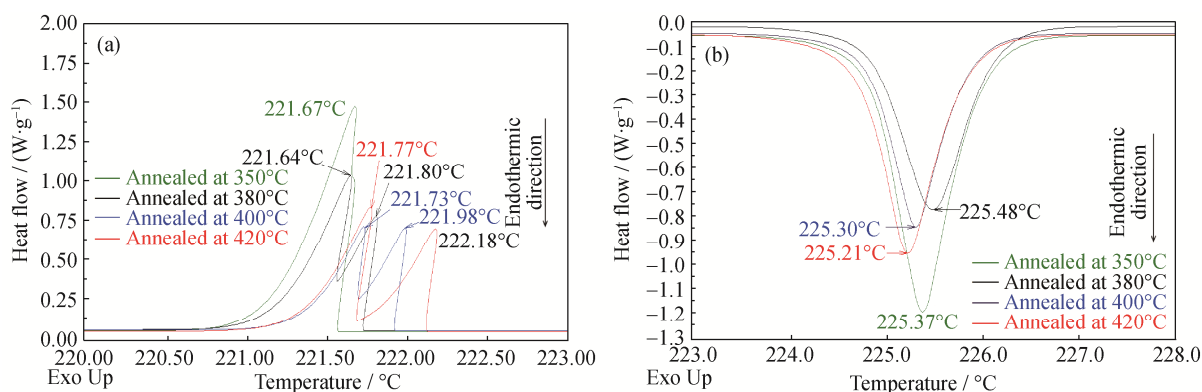


Fig. 11. Superimposed DSC curves of AL-2 SMA specimens annealed at various temperature: (a) cooling; (b) heating. Reprinted by permission from Springer Nature: *Journal of Thermal Analysis and Calorimetry*, DSC analysis of Cu–Zn–Sn shape memory alloy fabricated via electrodeposition route, R.D.V. Espiritu and A.V. Amorsolo Jr., Copyright 2012.

3.7. XRD analysis

The shim brass substrate was analyzed by XRD; the diffractograms corresponding to before and after annealing are shown in Fig. 12. The XRD patterns revealed five characteristic peaks for the shim brass, which were similar in position in both in the unannealed and annealed samples. This result verified that no changes occurred in the crystal structure of the brass substrate as a result of annealing and further confirmed that the brass substrate did not exhibit shape memory properties. The peaks, however, became narrower after annealing, indicating stress relief. Nonuniform strains in crystals are known to cause peak broadening; in our case, these strains might be due to cold working during the manufacturing process of the commercial shim brass.

Fig. 13(a) shows that the XRD patterns of the annealed Sn-brass samples had additional peaks not originally present in the patterns of the as-plated samples. The intensity of Sn peak decreased as the annealing time increased from 90 min to 120 min, suggesting enhanced diffusion and transformation to ternary intermetallics. These new peaks that correspond to the intermetallic phases produced

Because the transformation temperature was essentially constant under each temperature regime (i.e., austenite start/finish, martensite start/finish), the compositions of the intermetallic layer were essentially the same regardless of the annealing temperature employed. Fig. 11 also shows decreasing energies of both the $M \rightarrow A$ and the $A \rightarrow M$ transformation; however, the disparity between the ΔH values was not substantial. Such a difference between the ΔH values for all of the annealed AL-2 specimens was attributable to excess Sn deposited onto the surface.

after annealing were responsible for the shape memory behavior of the ternary alloy. As new peaks evolved in the patterns of the annealed samples, some distinguishable intensity peaks of Sn observed in the patterns of the as-plated samples disappeared in the patterns of the annealed samples, which also confirmed the formation of the intermetallic phases. We observed that only a single type of intermetallic compound was formed for all the annealed samples.

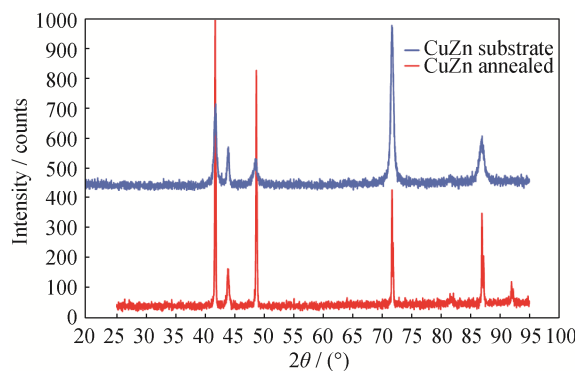


Fig. 12. Superimposed X-ray diffraction patterns of the shim brass and the annealed sample.

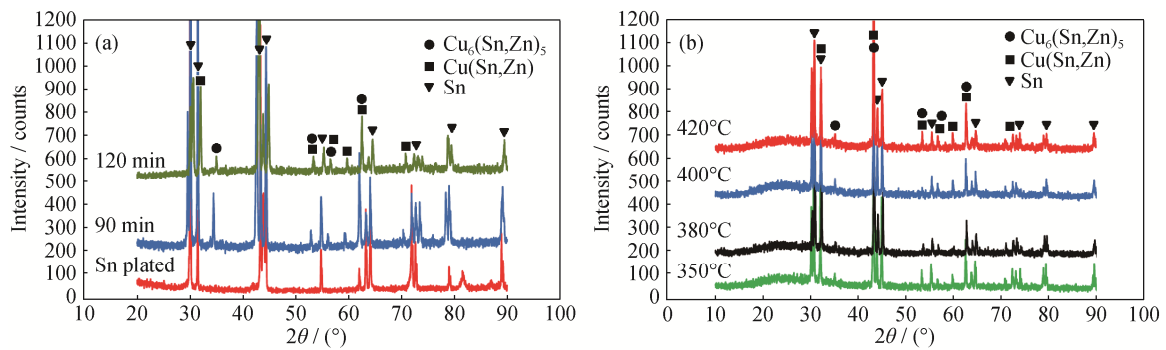


Fig. 13. Superimposed XRD patterns: (a) AL-3 plated and annealed at 400°C; (b) AL-2 heat-treated for 120 min at increasing annealing temperature.

Peaks in the diffractogram were consistent with the presence of Cu_6Sn_5 , although these intermetallics likely involve substitutional Zn in the lattice sites occupied by Cu and/or Sn given that Zn was a major constituent of the alloy. A preponderance of Sn peaks was still observed in the patterns of the annealed samples because not all of the plated Sn interdiffused with the brass substrate, as confirmed by the SEM analysis (Fig. 5). This lack of complete interdiffusion was also why peaks of the intermetallic phases were more prominent in the XRD patterns corresponding to specimens with lower Sn content than in those with higher Sn content. The excess amount of Sn on the surface masks the peaks of the intermetallic layers because the XRD technique was biased for signals from the surface region, which were less absorbed than those originating from deeper in the sample.

AL-2 strips annealed at various annealing temperature were also analyzed by XRD to verify the effect of increasing annealing temperature on the intermetallic phase formation by examining their characteristic peaks (Fig. 13(b)). The diffractogram clearly showed that annealing the Sn-plated alloy at higher temperature did not lead to additional peaks as compared with the patterns of the samples annealed at lower temperature. We observed, however, that peaks for samples annealed at higher temperature were relatively more intense than the peaks of the samples annealed at lower temperature. This greater intensity was attributed to intermetallic layer formation being more favorable at higher temperature, where interdiffusion of the constituent metals was enhanced. Additionally, Sn was still detected even at the highest annealing temperature of 420°C. We attributed this observation to the presence of undiffused Sn, which suggested that the annealing time of 120 min is insufficient for Sn to completely interdiffuse into the CuZn substrate.

The detection of $\text{Cu}_6(\text{Sn,Zn})_5$ intermetallics was confirmed by the EDS analysis. The Cu-to-Sn atomic ratio (Cu/Sn) in the Cu_6Sn_5 intermetallic was 1.20; therefore, the ratio of Cu/Sn for the resulting intermetallic phases in the

ternary alloy should have a comparable ratio. Because the average composition of the intermetallic layer, as determined by EDS, was 56.0at%, 36.1at%, and 7.9at% for Cu, Zn, and Sn, respectively (Table 3), the ratio of Cu/Sn for the intermetallic phase was 7.1, which was ca. 6 times greater than the Cu_6Sn_5 intermetallic. The Cu–Sn intermetallics likely contain Zn in their lattice; hence, the large observed discrepancy can be rationalized if the substitution of Zn into the Cu_6Sn_5 lattice was considered to produce a $\text{Cu}_6(\text{Zn,Sn})_5$ variant. The resulting ratio of Cu/(Zn and Sn) was calculated to be 1.27 (Table 3), which was similar to the Cu_6Sn_5 intermetallic.

4. Conclusions

Cu–Zn–Sn SMAs were successfully fabricated via an electrodeposition route in which brass substrates were plated with Sn and subsequently annealed. The fabricated SMAs had an average composition of 56.0at%, 36.1at%, and 7.9at% for Cu, Zn, and Sn, respectively, which was consistent with the literature for compositions of Cu–Zn–Sn alloys exhibiting shape memory properties. The shape memory response of the fabricated SMAs was tested and quantified via a flame test, where the highest displacement of 92.86% was obtained with increasing annealing temperature.

The transformation temperature—specifically, the A_s and M_s and temperature—was observed to be essentially constant at 225°C and 222°C, respectively. Thermal cycling of the fabricated SMAs led to consistent and reproducible martensitic phase recovery. Such high transformation temperature and reliable shape memory response indicated that the fabricated Cu–Zn–Sn SMAs were potentially suitable for specialized applications involving high-temperature service conditions.

The microstructural analysis of the annealed Sn-plated brass revealed the formation of a ternary alloy phase that thickened as the annealing temperature increased. The pro-

duced intermetallic layer, which was found to be responsible for the observed shape memory response, was formed chiefly by faster diffusion of Cu to Sn, with an activation energy of $34.82 \text{ kJ}\cdot\text{mol}^{-1}$, consistent with first-order martensitic transformation kinetics. XRD analysis revealed that the intermetallic phases were composed of substitutional Zn in the lattice occupied by Cu and Sn, leading to the formation of $\text{Cu}(\text{Zn},\text{Sn})$ and $\text{Cu}_6(\text{Zn},\text{Sn})_5$ intermetallic variants. However, the presence of excess Sn on the alloy surface and on the remaining unreacted brass substrate restricted the shape memory response of the fabricated SMAs. Thus, optimization of the Cu–Zn–Sn SMAs fabrication via our electrodeposition–annealing method should focus primarily on improving the annealing conditions (i.e., the annealing temperature and dwell time) to achieve complete interdiffusion of the metal constituents, enhance homogeneity of the ternary alloy, and, most importantly, obtain alloys that exhibit 100% strain recovery.

Acknowledgements

The authors acknowledge the Philippine Council for Industry, Energy and Emerging Technology Research and Development of the Department of Science and Technology (PCIEERD-DOST) for the research funding.

References

- [1] K. Otsuka and C.M. Wayman, *Shape Memory Materials*, Cambridge University Press, United Kingdom, 1999.
- [2] D.C. Lagoudas, *Shape Memory Alloys: Modeling and Engineering Applications*, Springer Science & Business Media, New York, 2008, p. 1.
- [3] J.M. Jani, M. Leary, A. Subic, and M.A. Gibson, A review of shape memory alloy research, applications and opportunities, *Mater. Des.*, 56(2014), p. 1078.
- [4] W.M. Huang, Z. Ding, C.C. Wang, J. Wei, Y. Zhao, and H. Purnawali, Shape memory materials, *Mater. Today*, 13(2010), No. 7-8, p. 54.
- [5] R.A. Ahmed, A comparative study on the corrosion performance of $\text{Ni}_{47}\text{Ti}_{49}\text{Co}_4$ and $\text{Ni}_{51}\text{Ti}_{49}$ shape memory alloys in simulated saliva solution for dental applications, *Acta Metall. Sin. (Engl. Lett.)*, 29(2016), No. 11, p. 1001.
- [6] L. Petrini and F. Migliavacca, Biomedical applications of shape memory alloys, *J. Metall.*, 2011(2011), art No. 501483
- [7] D. Quan and X. Hai, Shape memory alloy in various aviation field, *Procedia Eng.*, 99(2015), p. 1241.
- [8] S. Wang, K. Tsuchiya, L. Wang, and M. Umemoto, Deformation mechanism and stabilization of martensite in TiNi shape memory alloy, *J. Mater. Sci. Technol.*, 26(2010), No. 10, p. 936.
- [9] B.C. Zhang, J. Chen, and C. Coddet, Microstructure and transformation behavior of in-situ shape memory alloys by selective laser melting Ti–Ni mixed powder, *J. Mater. Sci. Technol.*, 29(2013), No. 9, p. 863.
- [10] H.J. Jiang, S.S. Cao, C.B. Ke, X.P. Ma, and X.P. Zhang, Fine-grained bulk NiTi shape memory alloy fabricated by rapid solidification process and its mechanical properties and damping performance, *J. Mater. Sci. Technol.*, 29(2013), No. 9, p. 855.
- [11] C.Y. Chung and C.W.H. Lam, Cu-based shape memory alloys with enhanced thermal stability and mechanical properties, *Mater. Sci. Eng. A*, 273-275(1999), p. 622.
- [12] R. Dasgupta, A look into Cu-based shape memory alloys: Present scenario and future prospects, *J. Mater. Res.*, 29(2014), No. 16, p. 1681.
- [13] E. Patoor, D.C. Lagoudas, P.B. Entchev, L.C. Brinson, and X.J. Gao, Shape memory alloys, Part I: General properties and modeling of single crystals, *Mech. Mater.*, 38(2006), No. 5-6, p. 391.
- [14] S. Ozgen and C. Tatar, Thermoelastic transition kinetics of a gamma irradiated CuZnAl shape memory alloy, *Met. Mater. Int.*, 18(2012), No. 6, p. 909.
- [15] H. Funakubo and J.B. Kennedy, *Shape Memory Alloys*, Gordon and Breach Science Publishers, New York, 1987.
- [16] M. Ahlers, Martensite and equilibrium phases in CuZn and CuZnAl alloys, *Prog. Mater. Sci.*, 30 (1986), No. 3, p. 135.
- [17] D.Y. Li, S.L. Zhang, W.B. Liao, G.H. Geng, and Y. Zhang, Superelasticity of Cu–Ni–Al shape memory fibers prepared by melt extraction technique, *Int. J. Miner. Metall. Mater.*, 23(2016), No. 8, p. 928.
- [18] Z.G. Wang, X.T. Zu, and Y.Q. Fu, Review on the temperature memory effect in shape memory alloys, *Int. J. Smart Nano Mater.*, 2(2011), No. 3, p. 101.
- [19] S. Miyazaki and K. Otsuka, Development of shape memory alloys, *ISIJ Int.*, 29(1989), No. 5, p. 353.
- [20] U. Sari, Influences of 2.5wt% Mn addition on the microstructure and mechanical properties of Cu–Al–Ni shape memory alloys, *Int. J. Miner. Metall. Mater.*, 17(2010), No. 2, p. 192.
- [21] G.B. Narasimha and S.M. Murigendrappa, Effect of zirconium on the properties of polycrystalline Cu–Al–Be shape memory alloy, *Mater. Sci. Eng. A*, 755(2019), p. 211.
- [22] X. Hu, Y.F. Zheng, Y.X. Tong, F. Chen, B. Tian, H.M. Zhou, and L. Li, High damping capacity in a wide temperature range of a compositionally graded TiNi alloy prepared by electroplating and diffusion annealing, *Mater. Sci. Eng. A*, 623(2015), p. 1.
- [23] P. Fricoteaux and C. Rousse, Nanowires of Cu–Zn and Cu–Zn–Al shape memory alloys elaborated via electrodeposition in ionic liquid, *J. Electroanal. Chem.*, 733(2014), p. 53.
- [24] İ.H. Karahan and R. Özdemir, Effect of Cu concentration on the formation of $\text{Cu}_{1-x}\text{Zn}_x$ shape memory alloy thin films, *Appl. Surf. Sci.*, 318(2014), p. 100.
- [25] S. Pourkhorshidi, N. Parvin, M.S. Kenevisi, M. Naeimi, and H.E. Khaniki, A study on the microstructure and properties of

- Cu-based shape memory alloy produced by hot extrusion of mechanically alloyed powders, *Mater. Sci. Eng. A*, 556(2012), p. 658.
- [26] S.H. Kang, S.G. Hur, H.W. Lee, and T.H. Nam, Microstructures and transformation behavior of Ti–Ni–Cu shape memory alloy powders fabricated by ball milling method, *Met. Mater.*, 6(2000), No. 4, p. 381.
- [27] T.H. Nam and S.H. Kang, Effect of ball milling conditions on the microstructure and the transformation behavior of Ti–Ni and Ti–Ni–Cu shape memory alloy powders, *Met. Mater. Int.*, 8 (2002), No. 2, p. 145.
- [28] K. Mehrabi, M. Brunčko, A.C. Kneissl, M. Čolič, D. Stamenković, J. Ferčec, I. Anžel, and R. Rudolf, Characterisation of melt spun Ni–Ti shape memory Ribbons' microstructure, *Met. Mater. Int.*, 18(2012), No. 3, p. 413.
- [29] M. Izadinia and K. Dehghani, Microstructural evolution and mechanical properties of nanostructured Cu–Al–Ni shape memory alloys, *Int. J. Miner. Metall. Mater.*, 19(2012), No. 4, p. 333.
- [30] A. Agrawal and R.K. Dube, Methods of fabricating Cu–Al–Ni shape memory alloys, *J. Alloys Compd.*, 750(2018), p. 235.
- [31] M. Schetky, *Intermetallic Compounds*, John Wiley and Sons, New York, 1994, p. 529.
- [32] M. Schlesinger and M. Paunovic, *Fundamentals of Electrochemical Deposition*, 2nd Ed., Wiley Interscience, New Jersey, 2006.
- [33] E.A. Brandes and G. Brook, *Smithells Metals Reference Book*, 7th Ed., Butterworth-Heinemann, Oxford, 1992.
- [34] R.D.V. Espiritu and A.V. Amorsolo Jr., SEM-EDX analysis of intermetallic phases in a Cu–Zn–Sn shape memory alloy, *Microsc. Anal.*, 24(2010), No. 6, p. 15.
- [35] M.S. Suh, C.J. Park, and H.S. Kwon, Growth kinetics of Cu–Sn intermetallic compounds at the interface of a Cu substrate and 42Sn–58Bi electrodeposits, and the influence of the intermetallic compounds on the shear resistance of solder joints, *Mater. Chem. Phys.*, 110(2008), No. 1, p. 95.
- [36] B.F. Dyson, T.R. Anthony, and D. Turnbull, Interstitial diffusion of copper in tin, *J. Appl. Phys.*, 38(1967), No. 8, p. 3408.
- [37] A. Churakova, D. Gunderov, A. Lukyanov, and N. Nollmann, Transformation of the TiNi alloy microstructure and the mechanical properties caused by repeated B2-B19' martensitic transformations, *Acta Metall. Sin. (Engl. Lett.)*, 28(2015), No. 10, p. 1230.
- [38] H.Y. Kim and S. Miyazaki, *Ni-Free Ti-Based Shape Memory Alloys*, Butterworth-Heinemann, Oxford, 2018, p. 193.
- [39] R.D.V. Espiritu and A.V. Amorsolo Jr., DSC analysis of Cu–Zn–Sn shape memory alloy fabricated via electrodeposition route, *J. Therm. Anal. Calorim.*, 107(2012), No. 2, p. 483.
- [40] T.W. Liu, Y.J. Zheng, and L.S. Cui, Transformation sequence rule of martensite plates and temperature memory effect in shape memory alloys, *Acta Metall. Sin. (Engl. Lett.)*, 28(2015), No. 10, p. 1286.